The Microstructure and Microchemistry of High Critical Current Nb$_3$Sn Strands Manufactured by the Bronze, Internal-Sn and PIT Techniques

P. J. Lee, C. M. Fischer, M. T. Naus, A. A. Squitieri, and D. C. Larbalestier

Abstract—Recent advances in Nb$_3$Sn conductor development have advanced the non-Cu critical current density, J_c, from 2000 A/mm^2 to almost 3000 A/mm^2 (12 T, 4.2 K). We have quantified a variety of state of the art composites for their microstructures using the fracture/Field Emission Scanning Electron Microscope, FESEM, technique and their microchemistry using Energy Dispersive X-ray Spectroscopy (EDS)/FESEM. The results of the measurements increasingly point to the importance of A15 composition in determining the critical current density as well as grain size. The highest critical current densities, however, are being attained by the internal Sn process which has yet to achieve as high a level of Sn (23–24.5 at.% Sn) in the A15 as for Powder-in-Tube (PIT) in which we measure as high as 25–26 at.% Sn. When Sn diffuses into the Cu stabilizer, it is found to have a great affinity for Nb$_3$Sn formation than dissolution into the Cu. A15 forms at the Nb-stabilizer surface with local Cu concentrations within the grains of the stabilizer of less than 0.1 at.% Cu. Elevated levels of Sn, however, were observed at the Cu grain boundaries. Both the quantified variations in composition and the peak levels of Sn indicate that further increases in performance should be expected.

Index Terms—Microstructure, Nb$_3$Sn, strand, superconducting materials.

I. INTRODUCTION

HIGH performance Nb$_3$Sn strands can now be fabricated with non-Cu critical current densities (J_c) in excess of 2200 A/mm^2 at 12 T, 4.2 K using powder in tube (PIT) [1], and internal Sn methods [2], [3].

In assessing the capability of these techniques to provide further improvements in critical current density, it is important to characterize this material in terms of both chemistry and microstructure. This paper combines image analysis of macro- and microstructures with microchemical analysis in order to describe and contrast the properties of high performance PIT and internal Sn strands.

II. EXPERIMENTAL PROCEDURE

A. Strand Source and Heat Treatment

Powder in Tube (PIT) process Nb$_3$Sn was supplied in unreacted from by ShapeMetal Innovation, Holland. Modified Jelly Roll (MJR) and Rod-in-Tube (RIT) internal Sn strands were supplied in optimized reacted condition by OI-ST and IGC-AS respectively as part of the US-DOE Conductor Development Program [4]. Both internal Sn strands achieved critical current densities of 2200 A/mm^2 at 12 T and 4.2 K. The high J_c OI-ST MJR strand uses a Sn(Cu) alloy core and Nb-2 at.% Ti expanded sheet filaments. Both the Ta-PIT uses a Nb-4 at.% Ta alloy.

B. Electron Microscopy

Fractured cross-sections of the reacted strands were used to determine the grain size of the Nb$_3$Sn. Polished transverse cross-sections, for microchemical analysis by Energy Dispersive Spectroscopy (EDS), and for quantification of A15 areas in FESEM, were prepared by standard metallographic techniques.

Microscopy was performed in a LEO 1530 FESEM capable of 2.5 nm spatial resolution at 5 kV. Backscattered electron imaging was performed using a Robinson scintillator detector with a $<0.003Z$ atomic number discrimination. Microchemical analysis was performed using a Noran light element detector and PROZA corrected standardless analysis software. We believe the absolute accuracy of the atomic Sn% results using this technique is <1 at.%, based on analyses of bulk A15 samples fabricated from carefully measured Nb+Sn powder mixtures and from the analyses of Cu–Sn line compounds.

III. RESULTS AND DISCUSSION

A. A15 Layer Critical Current Densities

In Fig. 1 we compare the critical current densities in the A15 layers of low hysteresis loss ITER strands with those of optimized high J_c (low Cu : Sn ratio in nonstabilizer region) strands. In the PIT strands there exists a layer of very large Nb$_3$Sn grains around the core. This layer has very few grain boundaries to pin flux and support significant J_c, so we have excluded this area from our measurements. There is a spread in the layer J_c (J_{csc}) values for the low hysteresis loss strands with the internal Sn processed strands with higher values than the bronze process strands. The highest low hysteresis loss internal Sn value of J_{csc} (2250 A/mm^2) at 12 T and 4.2 K is 23% higher than the lowest.
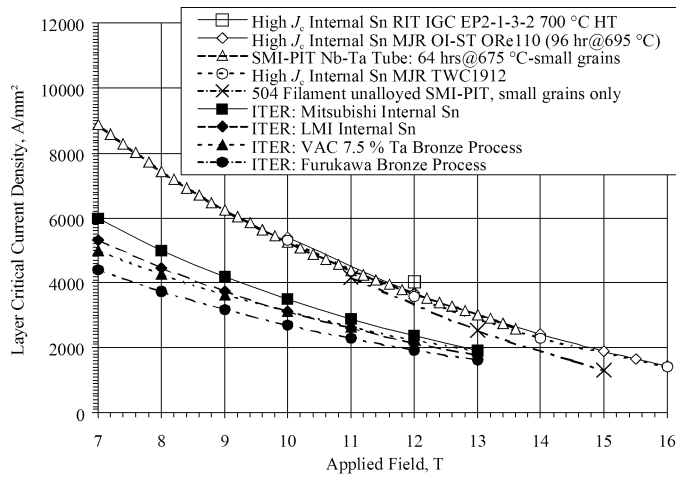
Fig. 1. Comparison of A15 layer critical current densities with field in high performance technical Nb₃Sn strands at 4.2 K. The ITER strands are designed for low hysteresis loss and are distinguished from "high J_c" strands by having a relatively large volume of Cu in the filament pack in order to separate the filaments. The "high J_c" designs have remarkably similar critical current densities in the A15 layer.
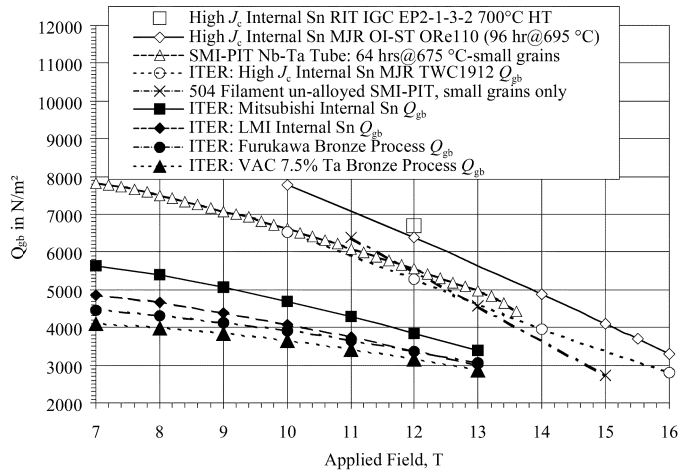

Fig. 2. Comparison of Q_{gb} with field in high performance technical Nb₃Sn strands at 4.2 K.

The J_{csc} values diverge toward lower field so that at 7 T (4.2 K) the highest internal Sn value (5990 A/mm²) is 36% more then the lowest bronze-process value. The optimized high-J_c strands have more similar J_{csc} values with the highest value at 12 T, 4.2 K (4030 A/mm²) only 13% higher than the lowest alloyed high J_c strand. The highest "high J_c strand" J_{csc} is 70% higher than the highest low hysteresis loss value. The J_{csc} values for the un-alloyed PIT strand are lower than for the other "high J_c" strands and have a steeper declining gradient in J_{csc} with field, such that an extrapolation of the J_{csc} to higher fields suggests a cross-over with low-hysteresis loss strands at ∼16 T.

B. Specific Grain Boundary Pinning Force

Using the mean grain boundary density, S_{GB}, of 0.018 nm⁻¹ and the filament J_c estimate for the point strand, we can calculate a value for the specific boundary pinning force, Q_{GB}, using Kramer's formalism [5]: $Q_{GB} = F_p / \lambda \, S_{gb}$ where λ is an efficiency factor which accounts for the proportion of the grain boundary that is oriented for pinning. Applying a value of 0.5

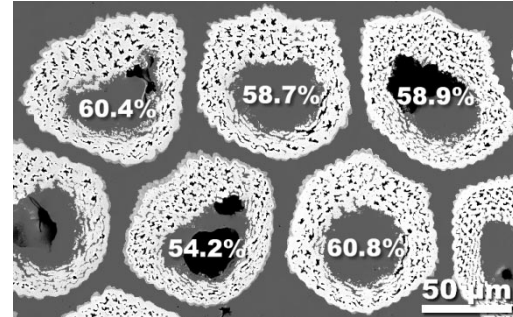| Wire Designation	Including Barrier Area			Excluding Barrier Area		
	Cu	Nb	Sn	Cu	Nb	Sn
ITER Internal Sn MJR (TWC 1721)	7.1	3.4	1.0	7.1	2.2	1.0
1ˢᵗ Generation High J_c Internal Sn MJR (TWC1912)	2.2	4.4	1.0	2.2	3.2	1.0
High J_c Internal Sn MJR (OI-ST 110)	2.3	3.3	1.0	2.3	2.3	1.0

Fig. 3. Variations in barrier reaction from sub-element to sub-element in a 2200 A/mm² (12 T, 4.2 K) internal Sn MJR strand (OI-ST 110) revealed by FESEM-BEI. Where large voids (Sn loss) occur in the core the barrier is less reacted. Superimposed on the sub-elements are the %A15 in the sub-elements. Nb dissolution into the core can also be observed as well as a thin layer of A15 on the outside of some of the filaments.

for λ, a value previously used for columnar grains, gives value of 270 N/m² measured at 5 T, 4.2 K for 2.1 nm thick α-Ti ribbons in conventional Nb-47wt.% Ti [6]. A similar separation of the "low-loss" and "high-J_c" strands is observed as in the case of the J_{csc}. A similar spread in Q_{gb} values is observed within the low-loss strands but a larger spread is now observed in the "high J_c" strands.

C. Overall Atomic Ratios of Cu, Nb and Sn

The contrast in Cu : Nb : Sn ratio (inside the non-Cu sub-element) between low-hysteresis loss and high-J_c is illustrated in Table I, which compares values for MJR Internal Sn strands derived from image analysis. In these "high J_c" (low sub-element Cu) composites the Nb barrier partially reacts, contributing to the J_c and utilizing some of the Sn. The 1st generation (TWC 1912) "high J_c" MJR is slightly Sn deficient (assuming a Nb : Sn target ratio of 3 : 1) but if the Nb diffusion barrier is included in the Nb area the ratio falls well below this level. The J_{csc} of this composite (Fig. 1) is still high although the Q_{gb} at 12 T, 4.2 K is 17% lower than the high-Sn "high-J_c" (OI-ST 110) MJR internal Sn composite.

D. Sub-Element Variations

1) MJR Internal Sn: Within the composites, there are variations in local A15 : Non-Cu ratios from sub-element to sub-element after reaction due to the large scale movement of Sn during reaction. In Fig. 3 we illustrate how the amount of reacted barrier varies with both position and Sn loss in the core. Where large voids occur in the core, the amount of barrier reacted is reduced and in cases where the core is void-free the barrier is
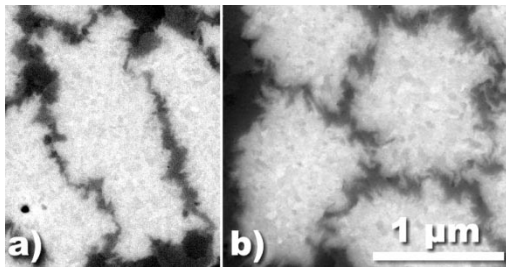
Fig. 4.   FESEM-BEI images of high-J_c (a) MJR expanded sheet filaments and (b) RIT internal Sn filaments prior to heat treatment.

fully reacted. These variations are superimposed on geometric distortions to the MJR sub-elements, which decrease the barrier thickness at the side and inward-facing edges of the sub-elements. Consequently, in these areas even sub-elements without large core voids can be fully reacted through. Fully reacting the barrier results in Sn diffusion into the stabilizer, which reduces the RRR. Nb dissolution into the core can also be observed.

Where large voids occur in the core there is also a reduced volume of reacted A15. There is an 11% variation in A15/Sub-element ratio across the five sub-elements shown in Fig. 3, with the lowest areas of A15 in the sub-elements with large interior voids.

2) PIT Strands: The PIT conductor consists of well-separated individual filaments in which the Nb tube from which the A15 is formed also serves as the diffusion barrier. The degree of filament uniformity is remarkable and is comparable to multifilamentary Nb-Ti strand (coefficient of cross-sectional area variation <5%). As in Nb–Ti strand, the largest filament distortions are seen on the outside filaments, which are not fully supported by the filament/Cu composite pack. As the reaction proceeds radially from the core, any distortion of the filaments results in premature react-through of the Nb at the narrowest filament width and poisoning of the stabilizer Cu surrounding the filament.

E. Microstructural Variations

Prior to heat treatment there is only a thin (0–150 nm) inter-filamentary layer of Cu in both MJR [Fig. 4(a)] and RIT [Fig. 4(b)] high-J_c internal Sn strands. There is also significant mechanical mixing of the Cu and Nb due to the plain strain deformation of the Nb grains. The grain size is larger and the inter-curling more pronounced in the RIT filaments than the expended sheet originated MJR filaments.

The "high J_c" internal Sn filaments join together during heat treatment to form a single mass of A15 enclosing voids and islands of Cu(Sn). Considering the exceptionally narrow pathways, it is remarkable how thoroughly reacted the composites can be. All the "high-J_c" MJR, RIT and PIT strands have similarly flat trends in A15 grain size across the layer [Fig. 5(a)]. The higher reaction heat treatment temperature (695 °C MJR and 700 °C RIT) internal Sn strands have larger A15 grain sizes than the PIT strands (heat treated at 675 °C). The A15 grain size (Feret diameter) in the IGC-AS RIT strand (70 hr/700 °C) is 33% greater than for the OI-ST MJR (96 hr/695 °C). The A15 grain size in the 4 at.% Ta alloy based PIT is greater than for the
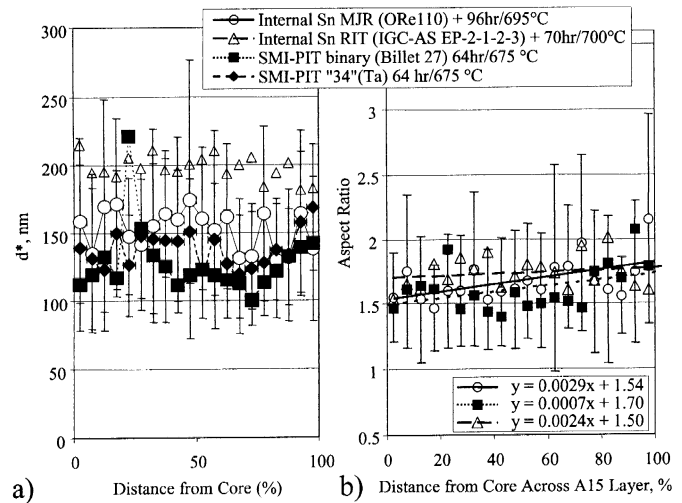

Fig. 5.   Variation in (a) A15 grain Feret diameter (d^*) and (b) aspect ratio with distance from core across A15 layer for optimized MJR and RIT internal Sn composites and two PIT composites. Each point spans 5% of the distance. Standard deviations for the OI-ST MJR composite are shown as vertical error bars. Linear fits for the aspect ratio trends are by least squares with the resulting equations shown below.
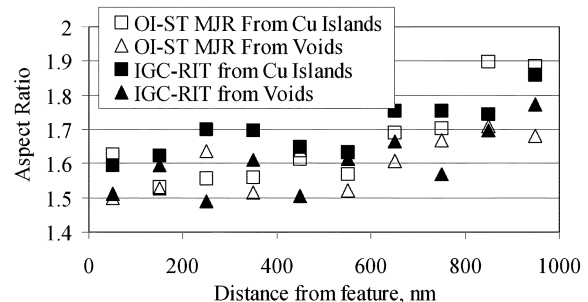

Fig. 6.   Variation in aspect ratio with distance from Cu islands and voids for "high-J_c" high Sn internal Sn MJR (OI-ST 110) and IGC-AS RIT (EP-2-1-2-3), (both 2200 A/mm^2 at 12 T, 4.2 K) A15 layer. Standard deviations 0.3–0.8.

unalloyed PIT. A shallow gradient in increasing A15 grain aspect ratio is observed across high-J_c and PIT layers as shown in Fig. 5(b). A columnar monolayer is observed on the outside edge for both MJR and PIT strands (for the MJR in the Nb diffusion barrier). If the outer 5% of the layer is excluded, the aspect ratio gradients shown in Fig. 4(b) drop by 41% for the MJR and by 8% for the PIT. An even lower gradient was observed across a high-J_c RIT internal Sn A15 layer (IGC-AS strand). The errors bars shown in Fig. 5(a) and b show the standard deviation for each data point where each data point represents 50 or more analyzed grains. It was found that increasing the sampling size beyond 50 grains did not reduce the standard deviation.

We have previously shown that the largest variations in A15 grain morphology, in a first generation high-J_c MJR strand, are found across the original filaments rather than across the A15 layer [7]. For the high Sn "high-J_c" OI-ST MJR and IGC-AS RIT analyzed here, we analyzed the variation in A15 grain morphology with respect to the distance from Cu(Sn) islands and voids (which by their nature define filament edges). In Fig. 6 we show for both the MJR and RIT strands there is little variation in A15 grain aspect ratio (an indicator of Sn supply) up to
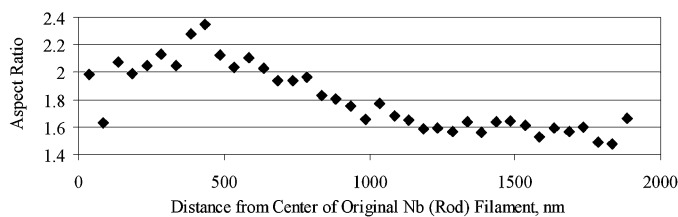
Fig. 7. A15 grain aspect ratio as a function of distance from the original filament centers in the IGC-AS RIT strand.
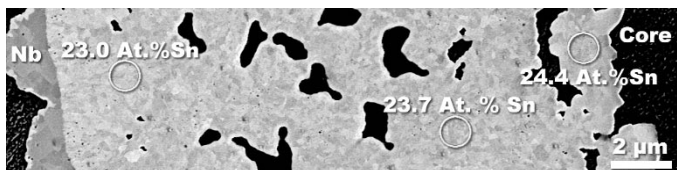

Fig. 8. FESEM-BEI image of A15 layer across in the optimized "high-J_c" MJR strand showing the key features in this material. The MJR filaments have formed a single layer of A15. A thin layer of A15 is formed on the outside of the Nb barrier (4) as a result react-through of the barrier.

a distance of 600 nm from the interface. After 600 nm there is a steady increase in aspect ratio, which is much more pronounced with distance from Cu islands for both strands.

The original filament centers areas were readily distinguished in the IGC-AS RIT internal Sn strands and a plateau in aspect ratio at ∼2 is reached 500–700 nm from the filament centers as shown in Fig. 7.

F. Microchemical Analysis

Microchemical analysis (ignoring Cu) by EDS indicates a compositional range in the high-J_c internal Sn MJR A15 layer from ∼24.5 at.% Sn near the Sn core to ∼23 at.% Sn near the Nb barrier for a J_c optimized heat treatment of 96 hrs at 695 °C. Using fractography to locate the original filament structure, a range of 21–24 at.% Sn was measured from filament centers to filament joins. The spatial resolution of this technique, however, is limited to ∼1 μm and consequently the local variation may be higher. An example of the key microchemical features found across the whole sub-element is shown in Fig. 8. A solid A15 layer is shown, formed from the original MJR filaments. On the outer surface of the Nb diffusion barrier, a thin layer of A15 is also formed, which results from Sn the reacting through of the diffusion barrier elsewhere. The A15 layer forms despite a measured Sn content in the stabilizer Cu of only 0.05–0.08 at.% Sn (values consistent with RRR measurements on this material). Differential etching of the Cu grain boundaries after barrier react-through suggests that Sn concentrates at the Cu grain boundaries. During heat treatment the Sn content of the core dropped to 0.15–0.22 at.% Sn.

The Sn composition in (SMI)PIT strand could be driven as high 25.2% Sn with high temperature heat treatment (800 °C). Relatively high Sn contents (∼7 at.% Sn) could still be measured in the core of the PIT filaments but the high Sn core was usually separated from the A15 layer by a void region. Using the same analysis conditions the compositions measured in low-hysteresis loss (ITER) internal Sn MJR was measured as 22–23 at.% Sn.

IV. CONCLUSION

Despite very small Cu layers between filaments, high Sn contents (23–24.5 at.% Sn) can be produced across the A15 layers in both MJR and RIT internal Sn strands. PIT strand can attain even higher levels of Sn concentration (24–25.5 at.%) for high temperature heat treatments. These values are significantly more than was produced in low-hysteresis-loss ITER strand (22–23 at.% Sn). A15 grain aspect ratio measurements, combined with EDS measurements, suggest that variations across the original 1–2 μm radius MJR and RIT filaments are similar to those across the entire final coalesced layer. In MJR internal Sn the Sn is efficiently removed from the core but large quantities of Sn are left in PIT cores.

REFERENCES

[1] J. L. H. Lindenhovius, E. M. Hornsveld, A. den-Ouden, W. A. J. Wessel, and H. H. J. ten-Kate, "Powder-in-tube (PIT) Nb$_3$Sn conductors for high-field magnets," *IEEE Trans. Appl. Superconductivity*, vol. 10, no. 1, pp. 975–978, March 2000.

[2] J. A. Parrell, Y. Zhang, R. W. Hentges, M. B. Field, and S. Hong, "Nb$_3$Sn strand development at Oxford superconducting technology," *Adv. Cryo. Eng.*, vol. 48B, pp. 968–977, 2002.

[3] E. Gregory and T. Pyon, "Internal tin Nb$_3$Sn conductor development for high energy physics applications," *Adv. Cryo. Eng.*, vol. 48B, pp. 958–967, 2002.

[4] R. M. Scanlan, D. R. Dietderich, and B. A. Zeitlin, "Development of cost-effective Nb$_3$Sn conductors for the next generation Hadron colliders," *Adv. Cryo. Eng.*, vol. 48B, pp. 949–957, 2002.

[5] E. J. Kramer, "Flux pinning in high-current-carrying superconductors," *Adv. Cryogenic Eng.*, vol. 28, pp. 307–322, 1982.

[6] P. J. Lee and D. C. Larbalestier, "Development of nanometer scale structures of Nb–Ti and their effect on the superconducting critical current density," *Acta. Met.*, vol. 35, pp. 2526–2536, 1987.

[7] P. J. Lee, C. D. Hawes, M. T. Naus, A. A. Squitieri, and D. C. Larbalestier, "Compositional and microstructural profiles across Nb$_3$Sn filaments," *IEEE Transactions on Applied Superconductivity*, vol. 11, no. 1, pp. 3671–3674, 2001.